

# Parallax-Tolerant Image Stitching with Epipolar Displacement Field

Jian Yu, Yi Yu and Feipeng Da  
Southeast University

{yujian, yuyi, dafp}@seu.edu.cn

## Abstract

*Large parallax image stitching is a challenging task. Existing methods often struggle to maintain both the local and global structures of the image while reducing alignment artifacts and warping distortions. In this paper, we propose a novel approach that utilizes epipolar geometry to establish a warping technique based on the epipolar displacement field. Initially, the warping rule for pixels in the epipolar geometry is established through the infinite homography. Subsequently, the epipolar displacement field, which represents the sliding distance of the warped pixel along the epipolar line, is formulated by thin plate splines based on the principle of local elastic deformation. The stitching result can be generated by inversely warping the pixels according to the epipolar displacement field. This method incorporates the epipolar constraints in the warping rule, which ensures high-quality alignment and maintains the projectivity of the panorama. Qualitative and quantitative comparative experiments demonstrate the competitiveness of the proposed method in stitching images large parallax.*

## 1. Introduction

Image stitching is a powerful technique that has already made significant contributions in various fields such as autonomous driving, medical imaging, surveillance video, and virtual reality. It involves combining multiple images with a limited field of view to create a scene with a wider field of view. Despite the significant progress made in image stitching techniques over the past few decades, generating high-quality panoramic images remains a challenge, particularly when dealing with images with large parallaxes.

Image stitching commonly employs a  $3 \times 3$  homography matrix, which represents a 2D projection transform, for image alignment. However, real-world scenes are often non-planar, or the viewpoints are not co-located, rendering a single global homography projection model inadequate in describing the required transformations. As a result, image misalignment or ghosting effects may occur.

To mitigate parallax artifacts, representative existing methods include adaptive warping algorithms and shape preservation methods. Adaptive warping algorithms segment the image and employ distinct warping models [6, 12, 14, 32, 34] for different regions to optimize the warping process using an energy minimization framework, thus reducing parallax artifacts [14, 34]. Nevertheless, the use of multiple homography transformations may introduce inconsistencies among the perspective transformations, which can impact the natural appearance of the overall stitched image.

Shape preservation methods aim to maintain both local and global geometric formations by leveraging geometric features, leading to improved stitching outcomes. Prominent geometric features, including frequently used feature points and line segments that retain the linear structure of an image, form substantial constraints for homography estimation when combined in image stitching [9, 15, 16, 30]. Additionally, more intricate geometric features, such as edge contours [5], depth maps [17] and semantic plane regions [13], are employed when designing diverse energy functions to enhance content alignment and shape preservation. Nonetheless, the suitability of these intricate designs in real-world applications necessitates considering factors like the availability of adequate geometric support for the scene and the computational efficiency of the algorithm.

Recently, techniques utilizing Convolutional Neural Networks (CNNs) for accurate homography estimation and stitching have emerged gradually. These methods discard geometric features in favor of high-level semantic features that can be flexibly learned using supervised [21, 24, 27], weakly supervised [28], or unsupervised [23] approaches. Although these methods deliver robust performance in stitching images with small baselines, they encounter difficulties when handling substantial parallax and conditions involving different datasets and resolutions.

Upon examining the aforementioned methods, it is evident that they are no longer reliant on fixed projection models. Instead, they adapt the models based on image data or salient geometric features in a data-driven manner, aiming to accurately align with the data. This approach effectively eliminates artifacts, but it also raises the possibility of vio-

lating projection principles during image stitching, resulting in the appearance of certain points in the stitched image that should not be projected due to foreground occlusion. This is more likely to occur in stitching scenarios with larger baselines. It is important to note that the views utilized for stitching still adhere to the rules of projection transformation and are subjected to strict epipolar geometry constraints.

Therefore, this paper proposes a parallax-tolerant stitching method based on the epipolar displacement field (EDF). Starting with the definition of planar induced homography, we deploy the homography-based warping model in the epipolar geometry of two views, establishing a warping method based on the infinite homography and epipolar geometry. This method establishes a mapping geometric relationship for image stitching in the epipolar geometry, correcting the projection relationship of the stitched images to satisfy the epipolar geometry constraint. Then, we draw on the idea of elastic local alignment (ELA) [14] and extend the local elastic deformation to the epipolar displacement field for image warping. The displacement field is created using the mathematical model of thin-plate splines (TPS) [25], whose parameters can be solved linearly according to the related theory of TPS. We use the model parameters to calculate the displacement of grid anchors in the image and generate the displacement field of the warped image through linear interpolation. Finally, the warped image is directly reprojected to generate seamless panoramic images. Overall, the algorithm retains the advantages of local deformation methods in accurately aligning image overlap regions, and introduces the epipolar constraint into the displacement field. It applies this constraint in the propagation process of the warping rule from the overlap to non-overlap regions, achieving projection consistency of panoramic images while eliminating disparity artifacts. This also preserves the shape to some extent, avoiding the computational costs associated with extracting lines or other complex features. The experimental results demonstrate that the proposed algorithm accurately aligns images with large parallax and exhibits advantages in both qualitative and quantitative comparisons.

The paper is organized as follows. In Section 2, the relevant literature on image stitching is discussed. Section 3 provides a detailed description of the proposed method, which includes deriving the plane-induced homography in epipolar geometry model, estimating the infinite homography, establishing the epipolar displacement field, and acquiring panoramic images. The results are presented and compared with other methods in Section 4. Section 5 concludes the paper.

## 2. Related Work

Extensive research has been conducted on the fundamental principles of image stitching in the domains of computer

vision and graphics. In this section, a concise survey is provided on adaptive warping methods, shape preservation methods, and recent advancements in deep learning.

### 2.1. Traditional Stitching

**Adaptive Warping Methods** Utilizing multiple homography transformations for adaptive alignment proves to be an effective approach in mitigating parallax artifacts. Gao [6] *et al.* introduced the dual-homography warping (DHW), where two homography matrices correspond to the perspective plane and the ground plane, and the stitching model is expressed as a combination of these two homography transformations. Zaragoza [32] *et al.* presented the As-projective-as-possible (APAP) algorithm, which partitions the image into grids and estimates a single homography for each grid to achieve alignment. Li [14] *et al.* employed robust elastic warping to mitigate parallax errors and devised a Bayesian feature refinement model to dynamically eliminate erroneous local matching in the grid. Lee [12] *et al.* substituted the spatial distance-based weights in APAP with warping residual weights and partitioned the input image into superpixels for adaptive warping. Nonetheless, the outcomes of this method are somewhat reliant on the accurate estimation of the initial multiple homographies.

Moreover, seam-driven image stitching [7, 19, 33] techniques endeavor to identify parallax-free local regions for precise alignment followed by the generation of high-quality seams for seamless stitching. Similar to adaptive warping methods, they strive to achieve superior alignment to eliminate parallax artifacts, but generally struggle to preserve the geometric structure information in the image.

**Shape Preservation Methods** Shape preserving methods aim to maintain both local and global geometries, resulting in visually pleasing seamless transitions. On one hand, methods such as shape-preserving half-projection (SPHP) [2], adaptive as-natural-as-possible (AANAP) warping [18], and global similarity prior (GSP) models [3] strive to enhance shape preservation by utilizing either local homography transformations or global similarity transformations. On the other hand, the combination of multiple geometric features in joint alignment can impose stronger constraints on homography estimation. Examples include the dual-feature warping (DFW) [15] based on point-line features, the single-perspective warping (SPW) [16], the line-guided local warping [30] with global similarity constraints, and the GES (GEometric Structure preserving)-GSP [5] which leverages edge features for a seamless transition between local alignment and shape preservation.

It should be noted that the aforementioned traditional methods lack a consistent projection model, and the resulting stitched images might contravene the principles of projection. Thus, the main purpose of this article is to guide image stitching in accordance with the rigorous principles

of projection.

## 2.2. Deep Learning Solution

Deep image stitching originates from the advancements in deep homography estimation. Since the initial proposal of deep homography estimation networks by DeTone [4] *et al.*, various supervised [1, 26], semi-supervised [10], and unsupervised [11, 20, 31] methods have been continuously proposed. These methods have demonstrated advanced performance in homography estimation, especially in scenarios with small baselines. However, significant room for improvement remains in wide-baseline scenes, particularly in those with multiple planes [10]. Deep image stitching methods employ homography estimation networks to estimate single [21, 24] or multiple homographies [22, 27] to warp images. Given the unavailability of ground truth stitching labels, unsupervised approaches are preferred [23]. However, further advancements are needed as the deep image stitching is still constrained by the limitations of deep homography estimation networks.

## 3. Method

In this section, we begin by deriving the plane-induced homography in the epipolar geometry. This allows us to establish the image warping formula based on the infinite homography and epipolar geometry. Next, we describe the process of retrieving the infinite homography under certain conditions, specifically for uncalibrated stereo rigs. Lastly, we construct an epipolar displacement field based on the warping model in the epipolar geometry and the theory of local elastic deformation. This field guides the target image to warp into the panorama, ensuring both accurate alignment and satisfaction of the epipolar constraints.

### 3.1. Plane Induced Homography

Image stitching utilizes planar homography to transfer points from one view to another view, as if they were projected onto one plane. Planar homography establishes the correspondence of image points between the two views, which is a form of projection relation closely associated with the two views' epipolar relationship. However, in many existing stitching methods, the use of multiple homographies for high-precision local alignment often results in projection distortion in non-overlapping regions, which hinders achieving better stitching quality. Alternatively, the adoption of a global similarity transformation method can also disrupt the epipolar relationship of particular points in non-overlapping regions. As demonstrated in Fig. 1, we labeled three epipolar lines and several points on each line in the target image for stitching. After applying existing stitching methods (*e.g.* APAP), we relabel these points and epipolar lines in the stitched image following the warping rules. In the overlapping region, the warped points still



Figure 1. Cases that fails to meet the epipolar constraint. Three epipolar lines, highlighted in yellow, along with several corresponding point sets, are identified in the upper half of the target image. However, the points that are transformed into the panoramic image using existing stitching methods no longer adhere to the epipolar lines as prescribed by the warping rule. This occurs mainly in the non-overlapping area.

satisfy the epipolar relationship, while the points in the non-overlapping region gradually deviate from the epipolar lines. Therefore, based on the plane-induced definition of homography, we propose a stitching model grounded in epipolar geometry that emphasizes the epipolar constraints in the stitched image.

Given a calibrated stereo rig, where the images in the two viewpoints are  $\mathcal{I}$  and  $\mathcal{J}$ . Suppose the camera matrices of the two views are with the world origin at the first camera,

$$\mathbf{P} = \mathbf{K}[\mathbf{I}|\mathbf{0}] \quad \text{and} \quad \mathbf{P}' = \mathbf{K}'[\mathbf{R}|\mathbf{t}] \quad (1)$$

where  $\mathbf{K}, \mathbf{K}' \in \mathbb{R}^{3 \times 3}$  are intrinsics (camera calibration matrix) of the two cameras.  $\mathbf{R} \in \text{SO}(3)$  and  $\mathbf{t} \in \mathbb{R}^3$  are the rotational matrix and translation vector from the second camera's coordinate frame to the world coordinate frames.

Suppose a plane  $\pi_E = (\mathbf{n}^T, d)^T$  in the world frame which does not contain either of the camera centers.  $\mathbf{n}$  is the normal vector of the plane and  $d/\|\mathbf{n}\|$  is the orthogonal distance of the plane from the first camera. Let  $\mathbf{X}$  be a world point on  $\pi_E$  so that  $\mathbf{n}^T \tilde{\mathbf{X}} + d = 0$ .  $\tilde{\mathbf{X}}$  represents the inhomogeneous coordinate of  $\mathbf{X}$ . The homography induced by  $\pi_E$  can be expressed as

$$\mathbf{H} = \mathbf{K}'(\mathbf{R} - \mathbf{t}\mathbf{n}^T/d)\mathbf{K}^{-1} \quad (2)$$

Since the epipole  $\mathbf{e}'$  on  $\mathcal{J}$  is  $\mathbf{K}'\mathbf{t}$  and replacing  $\mathbf{m}$  with  $-(\mathbf{n}^T/d)\mathbf{K}^{-1}$ , the homography in Eq. (2) can be further expanded as

$$\mathbf{H} = \mathbf{K}'\mathbf{R}\mathbf{K}^{-1} + \mathbf{e}'\mathbf{m}^T = \mathbf{H}_\infty + \mathbf{e}'\mathbf{m}^T \quad (3)$$

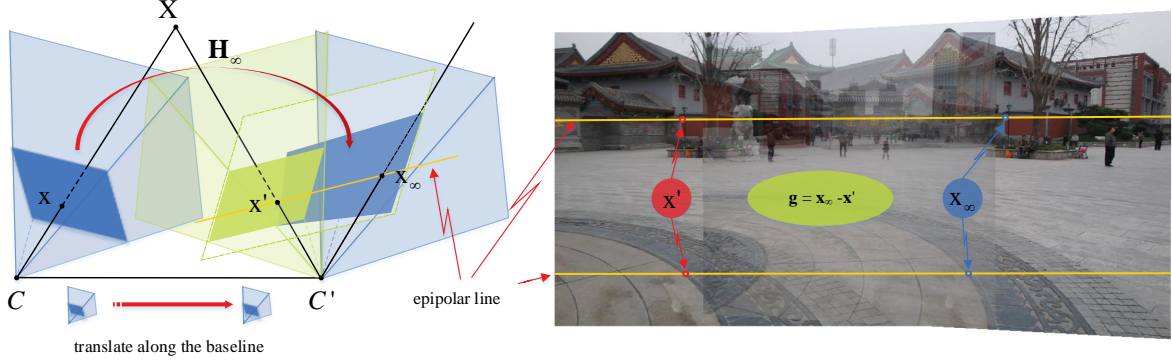


Figure 2. Warp image with the Epipolar Displacement Field. The transformation based on the infinite homography is equivalent to shifting the viewpoint of the object along the baseline direction of the stereo rig towards the reference viewpoint, forming a concentric projection model. In the image plane of the reference viewpoint, the warped image is formed by the intersection of the field of view from the new viewpoint and the reference image plane. In the stitching viewpoint, both  $\mathbf{x}_\infty$  and  $\mathbf{x}'$  lie on the epipolar line to maintain the epipolar constraint, while their distances give rise to the epipolar displacement field. With the help of this field, image warping aligns the pixels to the exact position along the epipolar lines.

where  $\mathbf{H}_\infty = \mathbf{K}'\mathbf{R}\mathbf{K}^{-1}$  is the infinite homography. Hence, the homography generated by a plane in space is a three-parameter family of homographies that are parameterized by  $\mathbf{m}$ . It is defined by the plane, camera intrinsic parameters, and relative extrinsic parameters. In addition,  $\mathbf{m}$  also represents the vanishing line of the  $\pi_E$  in  $\mathcal{I}$ .

### 3.2. Acquiring the Infinite Homography

To establish homography as defined by Eq. (3), we first need to obtain the infinite homography. If the aforementioned stereo rig is calibrated, such as scenarios those involving autonomous driving or security monitoring, the calibrated intrinsic and extrinsic parameters can be directly used to construct planar homography. However, for most image stitching cases, the rig is uncalibrated, which means that parameters such as the camera calibration matrix and rotation matrix.

For the camera intrinsic parameters, certain assumptions can be made, such as specifying an initial camera calibration matrix  $\mathbf{K}$ . The principal point coordinates can be approximated using the image's center point. Assuming equal horizontal and vertical focal lengths in terms of pixel dimensions. Their values can be estimated by examining the sensor chip size and lens focal length indicated in the image file header or by directly estimating a reasonable value. In the case of the stereo rig's extrinsic parameters, with the assumed initial  $\mathbf{K}$ , the rotation matrix can be obtained by decomposing the fundamental matrix  $\mathbf{F}$ , which can be calculated using RANSAC with the matched feature points  $\{\mathbf{x}_i, \mathbf{x}'_i\}$  in the images [8, 29]. Moreover, the coordinates of the epipoles  $e, e'$  in both views can be computed from the fundamental matrix according to  $\mathbf{F}\mathbf{e} = 0$  and  $\mathbf{F}^T\mathbf{e}' = 0$ . Finally, we optimize the aforementioned parameters using

an algorithm that minimizes the geometric distance of the images. Here, we construct an objective function by using a first-order approximation of the geometric error for optimization purposes [8]

$$\arg \min_{\mathbf{K}, \mathbf{K}', \mathbf{R}} \sum_i \frac{(\mathbf{x}_i^T \mathbf{H}_\infty \mathbf{F} \mathbf{x}_i)^2 + (\mathbf{x}'_i{}^T \mathbf{F} \mathbf{H}_\infty^{-1} \mathbf{x}'_i)^2}{(\mathbf{F} \mathbf{x}_i)_1^2 + (\mathbf{F} \mathbf{x}_i)_2^2 + (\mathbf{F}' \mathbf{x}'_i)_1^2 + (\mathbf{F}' \mathbf{x}'_i)_2^2} \quad (4)$$

where for instance  $(\mathbf{F} \mathbf{x}_i)_j^2$  represents the square of the  $j$ -th entry of the vector  $\mathbf{F} \mathbf{x}_i$ .

It is important to note that optimized solutions for  $\mathbf{K}, \mathbf{K}'$  and  $\mathbf{R}$  are not unique, as different initial values for  $\mathbf{K}, \mathbf{K}'$  generate varying results. This is because the mapping from the camera matrices to the fundamental matrix is not injective (one-to-one). While the fundamental matrix obtained from the feature point pairs relates to a series of possible camera matrices, the computation of  $\mathbf{H}_\infty$  is unique due to the requirement of satisfying the epipolar geometry constraint of  $\mathbf{H}_\infty^T \mathbf{F} = [\mathbf{e}]_x$ .  $[\ast]_x$  returns the skew-symmetric matrix of the input vector.

### 3.3. Warping via Epipolar Displacement Field

Transform  $\mathcal{I}$  into  $\mathcal{J}$  using the infinite homography. As shown in Fig. 2, the corresponding points of  $\mathbf{X}$  in  $\mathcal{I}$  and  $\mathcal{J}$  are denoted as  $\mathbf{x}$  and  $\mathbf{x}'$ , respectively. When  $\mathbf{X}$  is moved to infinity along its projection direction in  $\mathcal{I}$ , the projection of  $\mathbf{X}$  in  $\mathcal{J}$  will be  $\mathbf{x}_\infty$  transformed by the infinite homography. It can be seen that, in the epipolar plane where  $\mathbf{X}$  is located,  $\mathbf{x}$  in  $\mathcal{I}$  and  $\mathbf{x}_\infty$  in  $\mathcal{J}$  share the same direction of the counter-projection ray. Consequently, the transformation of  $\mathcal{I}$  through the infinite homography can be understood as moving the optical center of  $\mathcal{I}$  parallel along the baseline towards the optical center of the view  $\mathcal{J}$ . To further realize

the stitching of the two views, it is necessary to continue to adjust  $\mathbf{x}_\infty$  to  $\mathbf{x}'$  along the epipolar lines.

Based on the technique of robust elastic warping (REW), a thin plate spline curve with simple radial basis function (RBF) type is selected to warp the image in the case of given anchor points, providing good performance in terms of alignment quality and efficiency. REW assigns the residuals between the corresponding points  $\mathbf{x}'$  and  $\mathbf{x}_H = \mathbf{H}\mathbf{x}$  as  $\mathbf{g}$ , and aims to minimize these errors.  $\mathbf{H}$  denotes the global homography. Specifically, the residual  $\mathbf{g}(u, v) = (gx(u, v), hy(u, v))^T$  represents a deformation of the image, with  $g(u, v)$  and  $h(u, v)$  defining the deformations in the  $u$  and  $v$  directions, respectively, and being mutually independent. The alignment term  $J_D$  and the smoothness term  $J_S$  together form the energy function for the optimal warp, which are defined as

$$\begin{aligned} J_D &= \sum_{i=1}^N (g(u, v)^2 + h(u, v)^2) \\ J_S &= \iint_{(x, y) \in \Omega} |\nabla^2 \mathbf{g}|^2 dx dy \end{aligned} \quad (5)$$

The entire energy function uses the parameter  $\lambda$  to balance the two terms

$$J_\lambda = J_D + \lambda J_S \quad (6)$$

According to the regularization theory of TPS approximation, the deformation function can be represented as TPS interpolation, take the  $u$  direction as an example

$$g(u, v) = \sum_{i=1}^N \omega_i \phi_i(\mathbf{x}) + \alpha_1 u + \alpha_2 v + \alpha_3 \quad (7)$$

where  $\phi_i(\mathbf{x}) = |\mathbf{x} - \mathbf{x}_H|^2 \ln |\mathbf{x} - \mathbf{x}_H|$  is the RBF,  $\mathbf{w} = (\omega_1, \dots, \omega_n)^T$  and  $\mathbf{a} = (\alpha_1, \alpha_2, \alpha_3)^T$  are the coefficients.

Retrospectively examining Eq. (3), we can express  $\mathbf{x}'$  as  $\mathbf{H}_\infty \mathbf{x} + \mathbf{e}' \mathbf{m}^T \mathbf{x}$ , which, when represented in homogeneous coordinates, simplifies to  $\tilde{\mathbf{x}}' = \tilde{\mathbf{x}}_\infty + \tilde{\mathbf{e}}'$ . Importantly, it is observed that  $\mathbf{m}$ , a coefficient vector with three parameters, closely resembles the coefficient  $\mathbf{a}$  in Eq. (7). Thus, we can formulate a displacement field between  $\mathbf{x}_\infty$  and  $\mathbf{x}'$  with reference to the form of the residual  $\mathbf{g}$ . In this displacement field, all points are constrained to move along the corresponding epipolar lines. Therefore, we refer to it as an epipolar displacement field. These displacements can be expressed as

$$\begin{aligned} g(u, v) &= \sum_{i=1}^N \omega_i \phi_i(\mathbf{x}_\infty) + e'_1 (m_1 u + m_2 v + m_3) \\ h(u, v) &= \sum_{i=1}^N \varpi_i \phi_i(\mathbf{x}_\infty) + e'_2 (m_1 u + m_2 v + m_3) \end{aligned} \quad (8)$$

where  $\mathbf{w} = [\omega_1, \dots, \omega_N]^T$ ,  $\mathbf{w}' = [\varpi_1, \dots, \varpi_N]^T$  are the RBF's coefficients for the two directions of the image.  $e'_1, e'_2$  are the two elements of the inhomogeneous coordinates of the epipole  $\mathbf{e}'$ . These coefficient vectors can be computed through the following system of linear equations

$$\begin{aligned} (\mathcal{K} + \rho \mathbf{I}) \mathbf{w} + e'_1 \mathbf{M} \mathbf{m} &= [g_1(u, v), \dots, g_N(u, v)]^T \\ \mathbf{M}^T \mathbf{w} &= 0 \\ (\mathcal{K} + \rho \mathbf{I}) \mathbf{w}' + e'_2 \mathbf{M} \mathbf{m} &= [h_1(u, v), \dots, h_N(u, v)]^T \\ \mathbf{M}^T \mathbf{w}' &= 0 \end{aligned} \quad (9)$$

where  $\rho = 8\pi$  is a constant to adjust the interpolation [25],  $\mathcal{K}$  contains the set of RBFs  $\{\phi_i(\mathbf{x}_\infty)\}$ , and  $(M) = [\mathbf{x}'_i, \dots, \mathbf{x}'_N]^T$ .

Calculating the epipolar displacement field pixel-wise requires extensive computational resources. However, employing the approach outlined in APAP, we can partition the images into uniformly distributed grid cells and compute the displacement field of the cell vertices. Subsequently, interpolation can be utilized to ascertain the displacement field at every point within the cell.

In order to prevent the occurrence of holes in the distorted image domain that may arise when warping the pixels from view  $\mathcal{I}$  to view  $\mathcal{J}$ . Based on the obtained epipolar displacement field, we employ reverse warping from  $\mathcal{J}$  to  $\mathcal{I}$  to ultimately generate the panoramic image. It should be noted that during the stitching process, the warping rules of the overlapping region often suffer from over-fitting when propagated to non-overlapping areas. Specifically, the locally smooth warping can disrupt the global projection in the non-overlapping area. Nevertheless, in our approach, we did not incorporate the warping model with the global similarity transformation, as done in the REW method. The proposed epipolar displacement field, introduced in this paper, suppresses the deformation of the non-overlapping area through the application of global infinite homography and epipolar constraints. Fig. 3 demonstrates that the offset of each point from the epipolar line has been amended compared to the results obtained in Fig. 1.

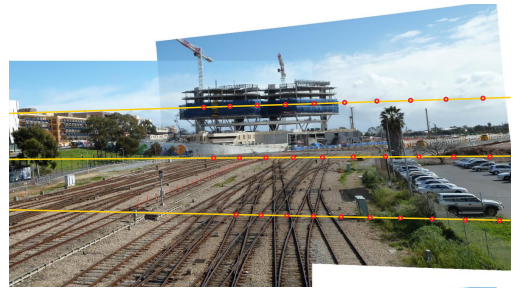


Figure 3. Epipolar constraints preservation: points on the epipolar line in the target image persist on the corresponding epipolar line after warping.

## 4. Experiment

In this section, we conduct a qualitative and quantitative comparison of the EDF method proposed in this article with existing methods to assess its stitching quality performance. The comparison includes global homography (GH), adaptive warping with multiple homographies (APAP [32]), the elastic deformation method (REW [14]), single-projective warping (SPW [16]), and the line-point consistent shape preserving warping (LPC [9]). The image pairs used in the experiments are primarily sourced from the literature of the aforementioned comparison methods.<sup>1</sup> These image pairs are primarily captured from different viewpoints with large baselines, resulting in significant parallax. Additionally, they all possess adequate overlapping regions to assess the alignment performance of the stitching methods.

In the experiments, we employed VLFeat for extracting and matching SIFT features of the images, utilized RANSAC to eliminate outliers in the feature points, and applied the eight-point method to compute the fundamental matrix of the stereo rig. As outlined in Sec. 3, our method initially estimated the camera’s intrinsic parameters to establish an initial calibration matrix  $\mathbf{K}$ . Subsequently, the infinite homography  $\mathbf{H}_\infty$  from the reference image to the target image was obtained through a geometric error optimization. Concerning the parameter configurations of the comparison methods, APAP partitioned the images into a  $100 \times 100$  cells, set the  $\sigma$  within the range of 8-12.5, and assigned  $\gamma = 0.01$ . The weighted parameter  $\lambda$  in REW was assigned a value of 0.1% of the product of the length and width of the image, while the smooth transition width in non-overlapping regions was set to five times the maximum bias. In LPC, the threshold  $\mu$  was established as 3 times the diagonal length of the grid. The  $\lambda_{lo}$  and  $\lambda_{gl}$  values in the energy function were set to 50 and 100, respectively. In addition,  $\lambda_p$  and  $\lambda_l$  were set to 1 and 5, and  $\lambda_{dg}$  and  $\lambda_{dn}$  are set to 50 and 100, correspondingly. SPW retains the identical parameters as LPC. To enable a comparison of alignment effects, all methods employed linear blending, with the exception of LPC, which utilizes a seam line for stitching.

### 4.1. Qualitative comparison

Fig. 4 illustrates the comparison of stitching results for a work table scene from the literature[14], displaying the sequential presentation of results from top to bottom: APAP, SPW, LPC, REW, and our method. The scene includes a calibration board with repetitive textures, and mismatches in these repetitive and structured patterns can cause pronounced distortion, thereby challenging the stitching algorithms. By zooming in on the chessboard section of the stitching results for each method, we observe multiple instances of misalignment and noticeable artifacts in both

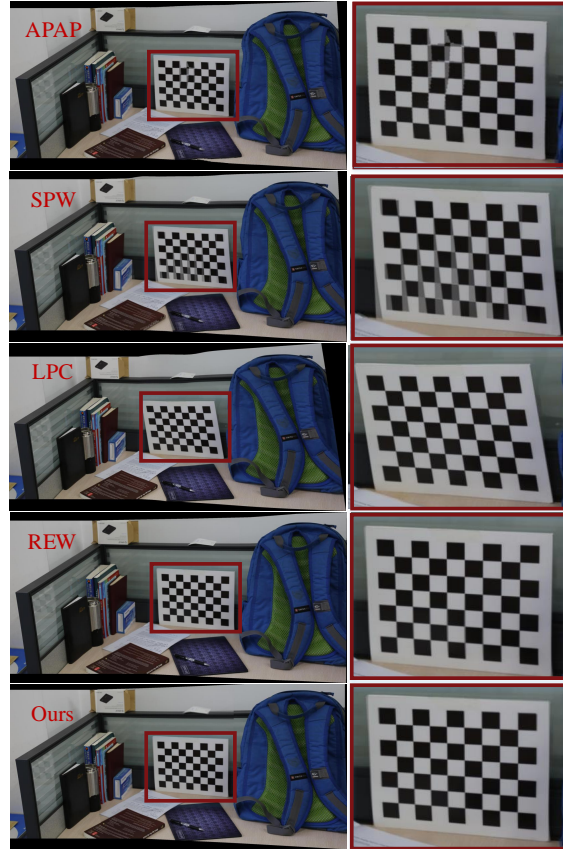


Figure 4. Comparison of stitching quality on a work table scene. From top to bottom are the results using APAP, SPW, LPC, REW and the method proposed in this paper. Where the checkerboard grid regions with repeated textures are extracted and enlarged to show the alignment performance of the different methods in this challenging scenario.

APAP and SPW. While LPC successfully aligns the target, it manifests bending deformation in the middle section on the top of the calibration board. Our method and REW yield comparable outcomes by accurately aligning the repetitive regions of the chessboard.

Fig. 5 displays additional scene comparisons, each column representing a scene consisting of temple [6], railtracks [32], garden [2], campus square [14] and cabin [14]. The temple and the railtracks are classic examples of large parallax stitching, whereas the other three exhibit similar characteristics, but with a smaller baseline distance between viewpoints and a larger direction gap. Each row in Fig. 5 corresponds to a method, and the stitching results of GH, APAP, REW, SPW, LPC, and the method proposed in this paper for five scenes are displayed from top to bottom. In summary, the latter four methods yield results with fewer artifacts, superior stitching outcomes compared to APAP, and enhanced robustness. It is important to note that APAP employs a

<sup>1</sup><https://github.com/dut-media-lab/Image-Stitching/tree/main/Imgs>



Figure 5. More Comparisons of the image stitching results obtained by the proposed method with GH, APAP, REW, SPW and LPC. The test image pairs are derived from the open source code of the literature [9]. From left to right, the order is temple, rail track, garden, campus square, and cabin.

Gaussian function to assign weights to each mesh, resulting in fluctuations in certain meshes. For instance, fluctuations can be observed in the mesh that contains the tower crane within the scene illustrated in the third row and second column of Fig. 5.

#### 4.2. Quantitative comparison

We employ Structural Similarity (SSIM) and Peak Signal-to-Noise Ratio (PSNR) as quantitative metrics to evaluate the registration quality of various methods. The tested images are obtained from publicly available data provided by references [6, 9, 14, 32]. Firstly, we detect and segment the overlapping region of the stitched images and calculate the SSIM and PSNR value for this region, which compares the reference and target images after stitching. The scores of

GH, APAP, SPW, REW, and our method in 10 large parallax image experiments are presented in Tab. 1, with the highest scores in each scenario highlighted in bold. Due to the seam line stitching employed by the LPC method, it is not included in the comparison presented in Tab. 1. The table reveals that the scores of REW and our method exhibit a close proximity and achieve the highest scores in certain scenarios, indicating effective alignment effects in the overlapping regions for both approaches. Given that both methods utilize TPS interpolation for constructing the deformation function, they demonstrate locally robust elastic registration. For maintaining fairness in the experiments, we employ the Multi-GS method for feature point matching across all methods to eliminate outliers, while not employing the Bayesian feature refinement model proposed in

Images			SSMI/PSNR		REW[14]	Ours
	GH	APAP[32]	SPW[16]			
DHW-temple	0.532/25.363	0.658/27.186	0.539/24.244	<b>0.801/29.657</b>	0.781/30.677	
APAP-railtrack	0.344/20.246	0.619/23.715	0.439/21.824	<b>0.790/27.118</b>	0.774/26.774	
REW-boardingbridge	0.566/28.258	0.615/29.300	0.611/29.190	0.619/24.126	<b>0.660/31.411</b>	
SPHP-park	0.597/25.651	0.648/26.007	0.624/24.130	0.663/21.144	<b>0.691/25.046</b>	
DFW-desk	0.879/26.029	0.906/27.094	0.882/26.218	<b>0.943/30.381</b>	<b>0.943/31.118</b>	
REW-campussquare	0.529/28.684	0.706/29.638	0.527/28.742	0.842/33.704	<b>0.861/34.258</b>	
SPHP-garden	0.454/25.248	0.565/26.115	0.551/26.092	0.633/25.238	<b>0.665/28.186</b>	
REW-cabin	0.441/20.682	0.728/25.241	0.529/21.930	<b>0.888/30.205</b>	0.852/28.463	
REW-gym	0.552/24.644	0.667/25.853	0.561/25.529	<b>0.869/30.996</b>	0.840/30.609	
REW-worktable	0.738/21.052	0.788/22.489	0.792/22.733	<b>0.920/28.932</b>	0.900/27.959	

Table 1. Comparisons on SSIM and PSNR.

REW, which has been demonstrated to enhance alignment effects.

### 4.3. Limitations

This method is primarily limited by the invisibility of spatial points from this particular perspective, which manifests in two different scenarios. First, when using a single perspective projection for stitching, the field of view larger than  $180^\circ$  becomes theoretically invisible and cannot be effectively stitched together. Second, there is the issue of invisibility caused by occlusion. Due to the implementation of a backward and reverse method, the inability to discern whether multiple points are projected onto the same location leads to an incapacity to detect occlusion. Fig. 6 illustrates several failed cases, where changes in the convergence of the perspective can readily lead to occlusions of the foreground objects between the two views, resulting in noticeable parallax artifacts. This convergence change mostly occurs when the perspectives' principal axes intersect forward.

## 5. Conclusion

This paper proposes a novel parallax-tolerant image stitching approach with the epipolar displacement field. Our approach first utilizes the infinite homography to establish a warping technique based on knowledge of epipolar geometry. The infinite homography aligns the target perspective with the reference perspective to form a concentric projection model, which ensures the warping of the target image pixels are performed along the associated epipolar lines. Subsequently, drawing inspiration from elastic local alignment, we extend the concept of local elastic deformation to generate an epipolar displacement field, which is then formulated with thin-plate splines. To expedite the calculation of the epipolar displacement field without compromising alignment accuracy, we establish a uniform grid on the

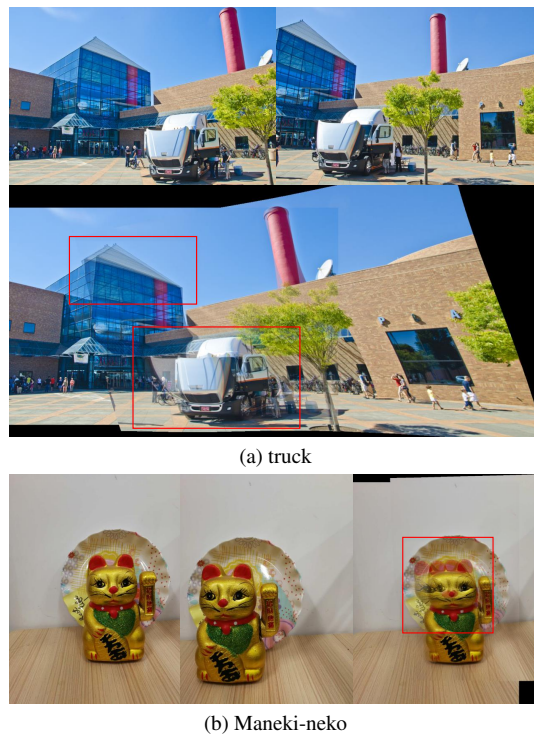


Figure 6. Failed cases were observed in scenarios due to severe occlusions in the input images. The identified artifacts in the resulting panoramas are highlighted with red circles.

image plane and obtain the displacement field through interpolation of the grid anchor points. Finally, the warped image is transformed using the displacement field to produce the stitched result. Through qualitative and quantitative comparative experiments, we evaluate the performance of the proposed method, which has high alignment quality for overlapping regions and preserves shape in non-overlapping regions through epipolar constraints.



## References

- [1] Si-Yuan Cao, Jianxin Hu, Zehua Sheng, and Hui-Liang Shen. Iterative deep homography estimation. In *CVPR*, pages 1879–1888, 2022. 3
- [2] Che-Han Chang, Yoichi Sato, and Yung-Yu Chuang. Shape-preserving half-projective warps for image stitching. In *CVPR*, pages 3254–3261, 2014. 2, 6
- [3] Yu-Sheng Chen and Yung-Yu Chuang. Natural image stitching with the global similarity prior. In *ECCV*, pages 186–201. Springer, 2016. 2
- [4] Daniel DeTone, Tomasz Malisiewicz, and Andrew Rabinovich. Deep image homography estimation. *arXiv preprint arXiv:1606.03798*, 2016. 3
- [5] Peng Du, Jifeng Ning, Jiguang Cui, Shaoli Huang, Xinchao Wang, and Jiabin Wang. Geometric structure preserving warp for natural image stitching. In *CVPR*, pages 3688–3696, 2022. 1, 2
- [6] Junhong Gao, Seon Joo Kim, and Michael S Brown. Constructing image panoramas using dual-homography warping. In *CVPR*, pages 49–56. IEEE, 2011. 1, 2, 6, 7
- [7] Junhong Gao, Yu Li, Tat-Jun Chin, and Michael S Brown. Seam-driven image stitching. In *Eurographics (Short Papers)*, pages 45–48, 2013. 2
- [8] Richard Hartley and Andrew Zisserman. *Multiple view geometry in computer vision*. Cambridge university press, 2003. 4
- [9] Qi Jia, ZhengJun Li, Xin Fan, Haotian Zhao, Shiyu Teng, Xinchen Ye, and Longin Jan Latecki. Leveraging line-point consistence to preserve structures for wide parallax image stitching. In *CVPR*, pages 12181–12190, 2021. 1, 6, 7
- [10] Hai Jiang, Haipeng Li, Yuhang Lu, Songchen Han, and Shuaicheng Liu. Semi-supervised deep large-baseline homography estimation with progressive equivalence constraint. In *AAAI*, pages 1024–1032, 2023. 3
- [11] Dewi Endah Kharismawati, Hadi Ali Akbarpour, Rumana Aktar, Filiz Bunyak, Kannappan Palaniappan, and Toni Kazic. Cornet: unsupervised deep homography estimation for agricultural aerial imagery. In *ECCV*, pages 400–417. Springer, 2020. 3
- [12] Kyu-Yul Lee and Jae-Young Sim. Warping residual based image stitching for large parallax. In *CVPR*, 2020. 1, 2
- [13] Aocheng Li, Jie Guo, and Yanwen Guo. Image stitching based on semantic planar region consensus. *IEEE TIP*, 30: 5545–5558, 2021. 1
- [14] Jing Li, Zhengming Wang, Shiming Lai, Yongping Zhai, and Maojun Zhang. Parallax-tolerant image stitching based on robust elastic warping. *IEEE TMM*, 20(7):1672–1687, 2018. 1, 2, 6, 7, 8
- [15] Shiwei Li, Lu Yuan, Jian Sun, and Long Quan. Dual-feature warping-based motion model estimation. In *ICCV*, pages 4283–4291, 2015. 1, 2
- [16] Tianli Liao and Nan Li. Single-perspective warps in natural image stitching. *IEEE TIP*, 29:724–735, 2019. 1, 2, 6, 8
- [17] Tianli Liao and Nan Li. Natural image stitching using depth maps. *arXiv preprint arXiv:2202.06276*, 2022. 1
- [18] Chung-Ching Lin, Sharathchandra U Pankanti, Karthikeyan Natesan Ramamurthy, and Aleksandr Y Aravkin. Adaptive as-natural-as-possible image stitching. In *CVPR*, pages 1155–1163, 2015. 2
- [19] Kaimo Lin, Nianjuan Jiang, Loong-Fah Cheong, Minh Do, and Jiangbo Lu. Seagull: seam-guided local alignment for parallax-tolerant image stitching. In *ECCV*, pages 370–385. Springer, 2016. 2
- [20] Ty Nguyen, Steven W Chen, Shreyas S Shivakumar, Camillo Jose Taylor, and Vijay Kumar. Unsupervised deep homography: A fast and robust homography estimation model. *IEEE Robotics and Automation Letters*, 3(3):2346–2353, 2018. 3
- [21] Lang Nie, Chunyu Lin, Kang Liao, Meiqin Liu, and Yao Zhao. A view-free image stitching network based on global homography. *Journal of Visual Communication and Image Representation*, 73:102950, 2020. 1, 3
- [22] Lang Nie, Chunyu Lin, Kang Liao, Shuaicheng Liu, and Yao Zhao. Depth-aware multi-grid deep homography estimation with contextual correlation. *IEEE TCSVT*, 32(7):4460–4472, 2021. 3
- [23] Lang Nie, Chunyu Lin, Kang Liao, Shuaicheng Liu, and Yao Zhao. Unsupervised deep image stitching: Reconstructing stitched features to images. *IEEE TIP*, 30:6184–6197, 2021. 1, 3
- [24] Lang Nie, Chunyu Lin, Kang Liao, and Yao Zhao. Learning edge-preserved image stitching from multi-scale deep homography. *Neurocomputing*, 491:533–543, 2022. 1, 3
- [25] Karl Rohr, H Siegfried Stiehl, Rainer Sprengel, Wolfgang Beil, Thorsten M Buzug, Jürgen Weese, and MH Kuhn. Point-based elastic registration of medical image data using approximating thin-plate splines. In *International Conference on Visualization in Biomedical Computing*, pages 297–306. Springer, 1996. 2, 5
- [26] Ruizhi Shao, Gaochang Wu, Yuemei Zhou, Ying Fu, Lu Fang, and Yebin Liu. Localtrans: A multiscale local transformer network for cross-resolution homography estimation. In *ICCV*, pages 14890–14899, 2021. 3
- [27] Dae-Young Song, Gi-Mun Um, Hee Kyung Lee, and Donghyeon Cho. End-to-end image stitching network via multi-homography estimation. *IEEE Sign. Process. Letters*, 28:763–767, 2021. 1, 3
- [28] Dae-Young Song, Geonsoo Lee, HeeKyung Lee, Gi-Mun Um, and Donghyeon Cho. Weakly-supervised stitching network for real-world panoramic image generation. In *ECCV*, pages 54–71. Springer, 2022. 1
- [29] Philip HS Torr and Andrew Zisserman. Mlesac: A new robust estimator with application to estimating image geometry. *Computer Vision and Image Understanding*, 78(1):138–156, 2000. 4
- [30] Tian-Zhu Xiang, Gui-Song Xia, Xiang Bai, and Liangpei Zhang. Image stitching by line-guided local warping with global similarity constraint. *PR*, 83:481–497, 2018. 1, 2
- [31] Nianjin Ye, Chuan Wang, Haoqiang Fan, and Shuaicheng Liu. Motion basis learning for unsupervised deep homography estimation with subspace projection. In *ICCV*, pages 13117–13125, 2021. 3

- [32] Julio Zaragoza, Tat-Jun Chin, Michael S. Brown, and David Suter. As-projective-as-possible image stitching with moving dlt. In *CVPR*, pages 2339–2346, 2013. [1](#), [2](#), [6](#), [7](#), [8](#)
- [33] Fan Zhang and Feng Liu. Parallax-tolerant image stitching. In *CVPR*, pages 3262–3269, 2014. [2](#)
- [34] Guofeng Zhang, Yi He, Weifeng Chen, Jiaya Jia, and Hujun Bao. Multi-viewpoint panorama construction with wide-baseline images. *IEEE TIP*, 25(7):3099–3111, 2016. [1](#)